

Energy Advances

Accepted Manuscript

This article can be cited before page numbers have been issued, to do this please use: M. Khan, A. Alshoaibi, A. Ali, Q. Liu, S. Khalida, M. Nazir, B. Sardar and M. Khan, *Energy Adv.*, 2026, DOI: 10.1039/D5YA00376H.



This is an Accepted Manuscript, which has been through the Royal Society of Chemistry peer review process and has been accepted for publication.

Accepted Manuscripts are published online shortly after acceptance, before technical editing, formatting and proof reading. Using this free service, authors can make their results available to the community, in citable form, before we publish the edited article. We will replace this Accepted Manuscript with the edited and formatted Advance Article as soon as it is available.

You can find more information about Accepted Manuscripts in the [Information for Authors](#).

Please note that technical editing may introduce minor changes to the text and/or graphics, which may alter content. The journal's standard [Terms & Conditions](#) and the [Ethical guidelines](#) still apply. In no event shall the Royal Society of Chemistry be held responsible for any errors or omissions in this Accepted Manuscript or any consequences arising from the use of any information it contains.

Metal-Organic Framework-Derived Ultra-Microporous Bismuth Oxide Synchronizing Energy Density and Stability in Symmetric Supercapacitors

Maaz Khan¹, Adil Alshoaibi², Atizaz Ali¹, Qi Liu¹, Syeda Khalida³, Maria Nazir⁴, Baseena Sardar⁵, Majid Khan^{5*}

¹School of Material Science and Engineering, Beijing Institute of Technology, Collaboration Center of Electric Vehicles in Beijing, Beijing 100081, China

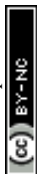
²Department of Physics, College of Science, King Faisal University, Al-Ahsa, 31982, Saudi Arabia

³Kohat University of Science and Technology, Kohat, Pakistan

⁴Ningbo Institute of Materials Technology and Engineering, Chinese Academy of Sciences, Ningbo 315201, China

⁵Department of Physics, Abdul Wali Khan University Mardan, Mardan 23200, Pakistan

* **Corresponding Author:** Dr. Majid Khan Email: majidkhan@awkum.edu.pk



Abstract

The development of bismuth oxide (Bi_2O_3) for supercapacitor applications is often limited by its intrinsically low electrical conductivity and structural instability during cycling. Herein, a metal–organic framework (MOF)-derived strategy is employed to engineer ultra-microporous Bi_2O_3 architectures with tailored structural and electrochemical properties. Through a controlled solvothermal synthesis followed by calcination using terephthalic acid as an organic linker, a hierarchically porous Bi_2O_3 structure is obtained with an enhanced surface area of $117 \text{ m}^2 \text{ g}^{-1}$ and dominant ultra-micropores centered at 0.42 nm . The engineered porous framework promotes efficient electrolyte infiltration and improved redox accessibility, resulting in a high specific capacitance of 876 F g^{-1} at 0.5 A g^{-1} in a three-electrode configuration. When assembled into a symmetric two-electrode supercapacitor operating within a $0\text{--}0.6 \text{ V}$ window, the MOF-derived Bi_2O_3 electrode delivers a device-specific capacitance of 950 F g^{-1} , achieving a maximum energy density of 47.2 Wh kg^{-1} at a power density of 150 W kg^{-1} . The device maintains 75.3% capacitance retention after $10,000$ charge/discharge cycles with a Coulombic efficiency of 81.4% . These findings demonstrate that MOF-assisted structural engineering effectively enhances ion transport pathways and electroactive surface utilization, offering a viable strategy for improving the electrochemical performance of metal oxide-based supercapacitors.

Keywords: Bismuth Oxide; Metal-Organic Frameworks (MOFs); Ultra-Microporous Materials; Symmetric Supercapacitors; Energy Storage

Introduction

The growing demand for energy, coupled with the swift advancement of the global energy needs, reduction of fossil fuels, escalating environmental concerns, and the increasing need for portable electronic devices, has created an urgent need for clean, sustainable, and efficient energy storage and conversion technologies [1]. In numerous domains, batteries, fuel cells, and supercapacitors represent the most effective and applicable technologies for the storage and conversion of electrochemical energy.

In recent decades, increasing attention has been directed toward supercapacitors due to their high-power density, rapid charge–discharge capability, and long cycle life. Their impressive electrochemical stability and fast energy delivery make them attractive for applications such as portable electronics, backup power systems, and hybrid electric vehicles [2].



Among various electrode materials, bismuth oxide (Bi_2O_3) has emerged as a promising candidate for supercapacitor applications due to its multiple oxidation states, rich redox activity, and environmental benignity [3]. However, the practical electrochemical performance of pristine Bi_2O_3 is often constrained by its relatively low electrical conductivity and limited structural stability during repeated charge/discharge cycles. These factors can reduce the effective utilization of electrochemically active sites and hinder charge transport under high-rate conditions. To overcome these challenges, researchers have explored nanostructuring strategies and composite formation to improve ion diffusion pathways, surface accessibility, and electrical conductivity [4].

Metal-organic frameworks (MOFs) have gained considerable attention as versatile precursors for synthesizing nanostructured metal oxides owing to their high porosity, tunable morphology, and large specific surface area [5]. MOF-derived Bi_2O_3 nanostructures inherit these advantageous characteristics, enabling enhanced electrolyte penetration, shortened ion diffusion distances, and increased exposure of redox-active sites, all of which are critical for efficient supercapacitor performance [6]. By carefully controlling the pyrolysis conditions of Bi-based MOFs, the crystallinity, pore architecture, and surface chemistry of the resulting Bi_2O_3 can be tailored, thereby optimizing charge storage behavior and rate capability [7].

Recent studies have demonstrated that MOF-derived Bi_2O_3 nanostructures exhibit superior electrochemical properties compared to conventionally synthesized Bi_2O_3 . For instance, porous Bi_2O_3 nanoflakes derived from Bi-MOFs have shown a high specific capacitance of 720 F g^{-1} at 1 A g^{-1} along with excellent cycling stability [8]. The interconnected porous network facilitates electrolyte penetration, while the nanostructured morphology shortens ion diffusion paths, contributing to enhanced rate capability [8].

Additionally, the incorporation of conductive materials such as carbon nanotubes or reduced graphene oxide further improves charge transfer kinetics, making MOF-derived Bi_2O_3 composites highly competitive for next-generation supercapacitors [9]. Despite these advancements, challenges remain in optimizing the synthesis parameters, understanding charge storage mechanisms, and scaling up production for commercial applications.

However, the effect of MOF structure on the electrochemical performance of Bi_2O_3 in supercapacitor applications has not been properly investigated. The incorporation of MOF-derived architectures into Bi_2O_3 can induce unique electronic and structural modifications that may address the inherent limitations of pristine Bi_2O_3 , such as its relatively low specific capacitance and



moderate electrical conductivity, which limit its effectiveness in energy storage devices [10]. By leveraging the structural features of MOF, it is anticipated to improve the electrochemical properties of Bi_2O_3 , overcoming the limitations and unlocking its full potential for high-performance supercapacitor applications.

This study presents the synthesis of MOF-derived Bi_2O_3 through a solvothermal-calcination method as a high-performance electrode material for supercapacitors. By reacting BiCl_3 with terephthalic acid (TPA) the resulting Bi_2O_3 MOF derivatives demonstrate enhanced electrochemical properties, including higher specific capacitance and improved charge storage, addressing the limitations of conventional Bi_2O_3 . The electrochemical performance of Bi_2O_3 and its MOF derivatives is compared using different characterizations. MOF-derived Bi_2O_3 in 1 M KOH electrolyte demonstrated a specific capacitance of 950 F g^{-1} at 0.5 A g^{-1} , excellent cyclic stability, high retention 75.3%, and a Coulombic efficiency of 81.4%, confirming it a promising symmetric supercapacitor candidate for efficient electrochemical energy storage devices.

Materials and Methods

Materials

Bismuth chloride (BiCl_3 , 98%), benzenetricarboxylic acid (95%), and N,N-dimethylformamide (DMF, 99.8%) were obtained at Sigma-Aldrich and used directly in the synthesis of the Bi_2O_3 and its MOF derivatives. All experiments used deionized (DI) water with resistivity $>18 \text{ M}\Omega\cdot\text{cm}$.

Synthesis of Bismuth Oxide (Bi_2O_3) Nanosheets

The step-by-step synthesis procedure of Bi_2O_3 nanosheets is illustrated in (Fig. 1a). Initially, 1.2 g of bismuth chloride (BiCl_3) was dissolved in 35 mL of ethylene glycol ($\text{C}_2\text{H}_6\text{O}_2$) under magnetic stirring at ambient temperature for 30 minutes until a clear and homogeneous solution was obtained (Solution 1). Ethylene glycol acted as a coordinating solvent and structure-directing agent during synthesis. The hydroxyl groups of ethylene glycol interact with Bi^{3+} ions, regulating hydrolysis and crystal growth, thereby promoting anisotropic growth and nanosheet formation. Additionally, its high boiling point and viscosity help control nucleation kinetics and suppress particle aggregation. Separately, 3.43 g of potassium hydroxide (KOH) was dissolved in 35 mL of ethylene glycol under vigorous magnetic stirring to form a transparent homogeneous solution (Solution 2). Then (Solution 2) was added dropwise to (Solution 1) under continuous stirring using



a burette, resulting in the formation of Solution 3. After complete addition, the reaction mixture was further stirred for 30 minutes to ensure uniform mixing and controlled nucleation, producing (Solution 4). The resulting mixture (Solution 4) was transferred into a 100 mL Teflon-lined stainless-steel autoclave and subjected to solvothermal treatment at 140°C for 12 hours. After naturally cooling to room temperature, the yellow Bi₂O₃ precipitate was collected and washed several times with ethanol and deionized water to remove residual impurities and by-products. The product was then dried under vacuum at 80°C. Finally, the dried powder was annealed at 500°C for 4 hours under an argon atmosphere to obtain calcined Bi₂O₃ nanosheets with enhanced crystallinity. The calcination step was performed to enable a direct comparison between calcined Bi₂O₃ and MOF-derived Bi₂O₃. Since MOF-derived Bi₂O₃ is obtained by calcining the Bi₂O₃-MOF at 500 °C for 4 hours under an argon atmosphere, the calcined Bi₂O₃ sample was prepared under similar thermal conditions to ensure a fair and systematic comparison of structural and electrochemical properties.

Synthesis of Bi₂O₃ Metal-Organic Framework Derivatives

The step-by-step synthesis procedure of MOF-derived Bi₂O₃ is illustrated in (Fig. 1b). Initially, 0.892 g of bismuth chloride (BiCl₃) was dissolved in 35 mL of N,N-dimethylformamide (DMF) under magnetic stirring for 30 minutes to obtain a clear and homogeneous solution (Solution A). Separately, 1.411 g of terephthalic acid (TPA) was dissolved in 35 mL of DMF and stirred for 30 minutes to form (Solution B). As shown in Fig. 1b, (Solution B) was slowly added to Solution A under continuous magnetic stirring. Upon mixing, coordination interactions occur between Bi³⁺ ions and the carboxylate groups of TPA. In the polar DMF medium, partial deprotonation of the carboxylic acid groups facilitates the formation of Bi–O–C coordination bonds, leading to the generation of homogeneous metal–ligand complexes and pre-nucleation clusters in solution (Solution C). Continuous stirring for an additional 1 hour ensures uniform coordination and prevents localized supersaturation, which is essential for controlled framework formation. The resulting homogeneous precursor solution (Solution C) was transferred into a Teflon-lined stainless-steel autoclave and subjected to solvothermal treatment at 150°C for 24 hours, promoting coordination-driven self-assembly and crystallization of the Bi-based MOF framework. After naturally cooling to room temperature, the obtained MOF precursor was collected and washed thoroughly with DMF, deionized water, and ethanol to remove residual reactants and impurities. The purified product was then dried at 80°C under an inert atmosphere.



Finally, the dried MOF precursor was calcined at 500°C for 4 hours under an argon atmosphere. During calcination, the organic linker decomposes while the inorganic Bi–O framework is retained, yielding porous MOF-derived Bi₂O₃.

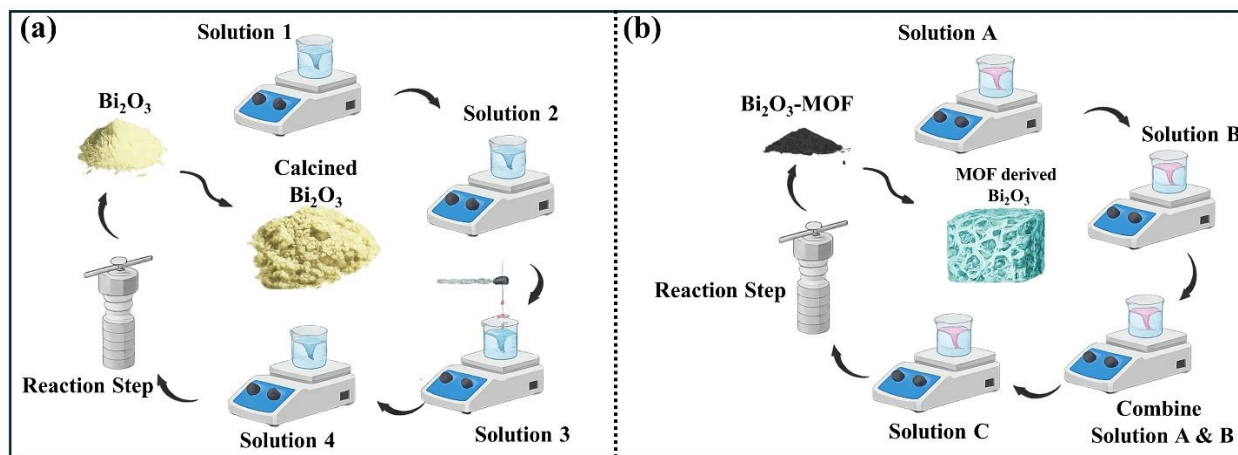


Fig. 1 Step-wise Solvothermal-Calcination synthesis flowchart of (a) Bi₂O₃ and (b) MOF-derived Bi₂O₃.

The physical characterization tools used in this work such as structural, morphological, compositional and textural analysis are all fully described in the (Supplementary Information File). Moreover, the specific guidelines to the electrode ink preparation, fabrication of a supercapacitor, and assembling a cell are also provided there. The underlying equations applied to calculate the structural parameters such as average Crystallite Size (nm), (%) Crystallinity, and electrochemical parameters like specific capacitance, energy density, power density, and impedance derived parameters are also reported in the (Supplementary Information) to make the results of the study, and the obtained results clear and reproducible.

Results and Discussions

Structural, Morphological and Elemental Analysis

The XRD patterns in (Fig. 2a) elucidate the structural evolution from the Bi-based MOF precursor to the final MOF-derived Bi₂O₃. The uncalcined sample (Bi-MOF) exhibits distinct diffraction peaks at 17.04°, 27.2°, and 41.89°, which correspond to the anorthic crystalline arrangement of terephthalic acid (TPA) linkers [11]. The presence of these organic linker peaks provides direct experimental evidence of a coordinated metal-organic framework structure, rather than a simple mixture of precursors. Upon calcination at 500°C, these TPA-related peaks completely disappear, confirming the thermal decomposition of the organic component. Concurrently, the pattern transforms to reveal the characteristic (110) peak of δ -Bi₂O₃ at 12.14°,



which aligns strongly with the cubic phase (PDF-2 # 00-005-0626). The retention of this typically metastable phase at room temperature is attributed to stabilizing factors such as oxygen-vacancy generation, kinetic trapping during cooling, and potential pinning by residual carbonaceous species from the decomposed MOF [12-16]. A detailed comparison with conventionally prepared Bi_2O_3 (Fig. 2b) reveals a systematic shift of diffraction peaks toward higher 2θ values in the MOF-derived sample, indicating measurable lattice contraction due to thermal-induced oxygen loss and strain development from the MOF template [17, 18].

Furthermore, the pronounced broadening of the (110) and (200) reflections in the MOF-derived Bi_2O_3 signifies substantial lattice disorder. This broadening is attributed to the preservation of mesoporosity upon linker removal, the development of micro-strain from defect clusters, and possible carbon substitution at oxygen-deficient sites [19]. The anisotropic suppression of specific crystallographic planes further suggests directionally-dependent strain effects from the oriented attachment of MOF-derived fragments. These collective structural transformations quantified by crystallite size and percentage crystallinity in (Table 1) demonstrate the complex interplay between MOF precursor chemistry and thermal history in engineering advanced Bi_2O_3 materials with tailored defect structures and enhanced functionality [11].

To measure the textural characteristics and pore structure of the synthesized samples, nitrogen (N_2) adsorption–desorption analysis was conducted at 77 K, as shown in (Fig. 2c). The specific surface areas were calculated using the Brunauer-Emmett-Teller (BET) method within the relative pressure (P/P_0) range of 0.05-0.30, while the pore size distribution was derived using the non-local density functional theory (NLDFT) model. The measured BET surface areas were $19 \text{ m}^2 \text{ g}^{-1}$, $15 \text{ m}^2 \text{ g}^{-1}$, $58 \text{ m}^2 \text{ g}^{-1}$, and $117 \text{ m}^2 \text{ g}^{-1}$ for pristine Bi_2O_3 , calcined Bi_2O_3 , Bi_2O_3 -MOF precursor, and MOF-derived Bi_2O_3 , respectively, indicating a substantial enhancement in surface area after MOF-assisted structural engineering. The MOF-derived Bi_2O_3 exhibits a hybrid Type I/Type IV isotherm with a pronounced hysteresis loop in the intermediate-to-high relative pressure region ($P/P_0 > 0.4$), confirming the coexistence of microporous and mesoporous structures. Furthermore, the gradual increase in nitrogen uptake as P/P_0 approaches 1.0 suggests the presence of macropores, likely formed due to interparticle voids and structural reconstruction during MOF decomposition and calcination. This confirms the formation of a hierarchical pore network consisting of ultramicropores, mesopores, and macropores [13-16]. A sharp uptake at low relative pressure ($P/P_0 < 0.1$) indicates significant microporosity. As shown in Fig. 2d, The NLDFT pore



size distribution reveals dominant ultramicropores centered at approximately 0.42 nm. From an electrochemical perspective, the relationship between pore size and electrolyte ion dimensions is particularly important. The hydrated diameter of K^+ ions in aqueous 1 M KOH is approximately 0.66–0.72 nm, which is larger than the measured ultramicropores size. However, under applied potential, partial desolvation of hydrated ions at the electrode/electrolyte interface may occur, allowing ion accommodation within confined pores. Additionally, OH^- ions, which possess comparatively smaller hydrated dimensions, may more readily access these ultramicroporous regions [13-16].

In this hierarchical architecture, ultramicropores contribute to enhanced surface charge accumulation and increased electrolyte/electrode interfacial interaction, while mesopores and macropores act as ion-buffering reservoirs and facilitate rapid ion diffusion and electrolyte penetration. This synergistic pore structure optimizes ion transport kinetics and charge storage efficiency, thereby improving electrochemical performance [20]. Such multiscale pore architectures have been widely reported to enhance charge storage behavior by maximizing accessible surface area while minimizing ion transport resistance [13-16]. These findings are consistent with recent reports on MOF-derived metal oxides possessing hierarchical porosity for advanced energy storage applications. The detailed BET surface area and pore parameters of the samples are summarized in (Table 1).



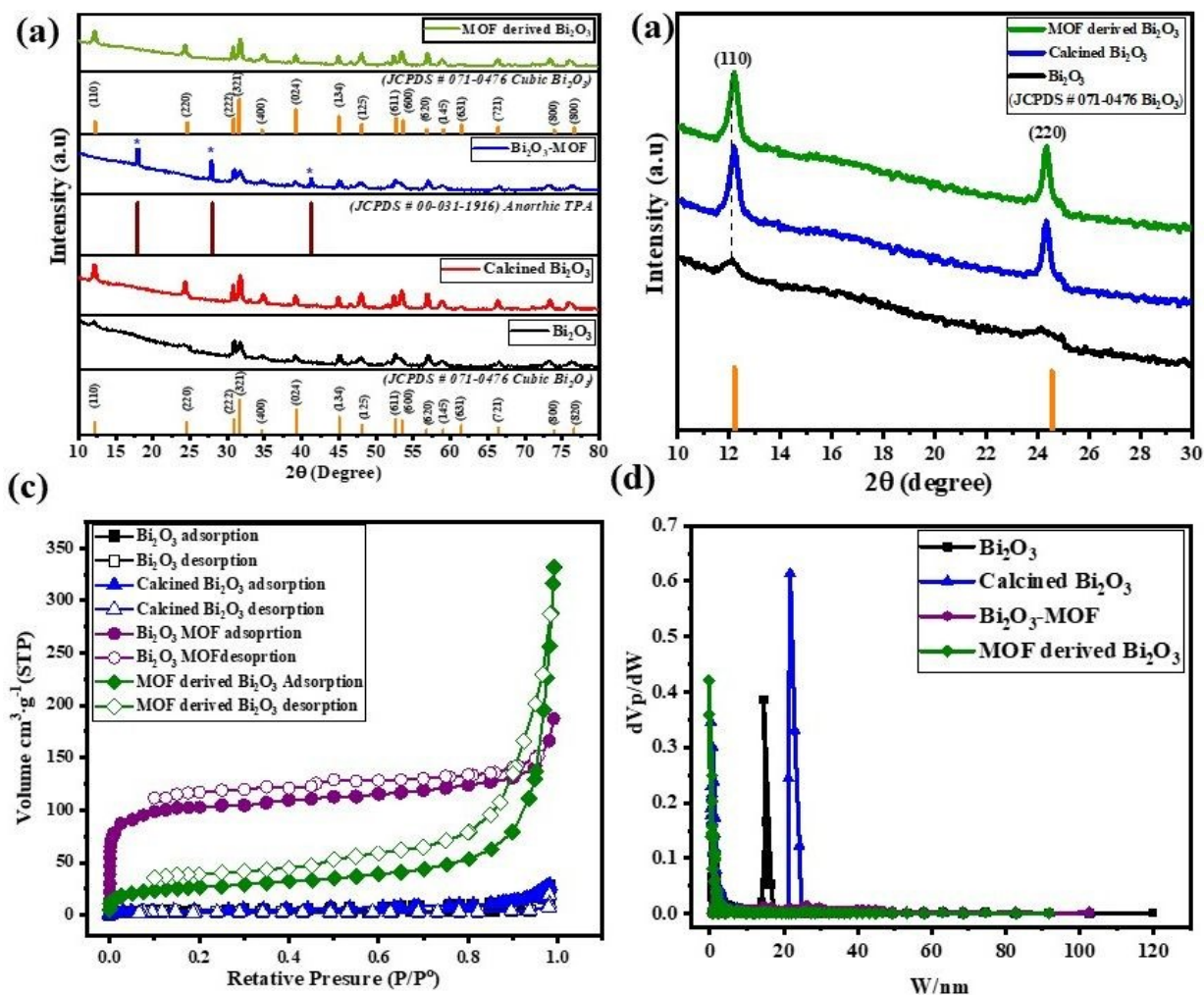


Fig. 2 (a) XRD patterns of Bi₂O₃ and its MOF derivatives within (10 - 80°) 2θ range and (b) XRD patterns of Bi₂O₃ and its MOF derivatives within (10 - 80°) 2θ range, (c) Brunauer–Emmett–Teller (BET) isotherms and (d) pore size distribution (PSD) of Bi₂O₃ and its MOF derivatives obtained through NLDFT model.

Table 1: Average crystallite size, % crystallinity, BET surface area and pore size distributions (PSD) of fabricated Bi₂O₃ and its MOF derivatives.

S. No	Samples Name	Average Crystallite Size (nm)	(%) Crystallinity	BET Active-Surface Area (m ² g ⁻¹)	Pore Size (PSD) (nm)
1	Bi ₂ O ₃	25	69.5	19	14.5
2	Calcined Bi ₂ O ₃	75	86.3	15	21.7
3	Bi ₂ O ₃ -MOF	24	75.7	58	1.40
4	MOF derived Bi ₂ O ₃	59	81.4	117	0.42



FT-IR spectroscopy was employed to investigate the bonding characteristics and surface functional groups of the synthesized samples. The FT-IR spectra are presented in (Fig. 3a). The characteristic absorption bands observed at approximately 512 cm^{-1} and 877 cm^{-1} are attributed to O–Bi–O stretching vibrations within the Bi_2O_3 lattice [21]. The band near 699 cm^{-1} corresponds to octahedral vibration modes associated with Bi–O bonds in Bi_2O_3 [18]. A pronounced peak at approximately 1387 cm^{-1} is assigned to surface-adsorbed carbonate species, which commonly arise from atmospheric CO_2 adsorption on metal oxide surfaces. A broad band observed at higher wavenumbers (around $3200\text{--}3500\text{ cm}^{-1}$) is attributed to surface hydroxyl groups and/or physically adsorbed water molecules [22]. For the Bi-based coordination precursor ($\text{Bi}_2\text{O}_3\text{--MOF}$), additional vibrational bands appear in the range of $700\text{--}1500\text{ cm}^{-1}$, which are absent in pristine Bi_2O_3 . These bands correspond to aromatic C=C stretching vibrations and symmetric/asymmetric stretching of carboxylate (COO^-) groups derived from the terephthalate linker [13-16]. The presence of these carboxylate-related peaks confirms coordination between Bi^{3+} ions and the organic linker during precursor formation [13-16]. After calcination at $500\text{ }^\circ\text{C}$, these organic-related vibrational bands disappear, indicating decomposition of the organic linker and formation of pure MOF-derived Bi_2O_3 [13-16]. A slight shift of Bi-O vibrational peaks toward higher wavenumbers in the calcined samples may be associated with improved crystallinity, reduced structural defects, and lattice rearrangement induced by thermal treatment. These observations are consistent with phase stabilization and structural refinement after annealing [23].

The X-ray Photoelectron Spectroscopy (XPS) survey spectrum of the MOF-derived Bi_2O_3 sample offers a detailed analysis of the elemental composition and surface chemical states. The survey spectrum as shown in (Fig. 3b) reveals multiple distinct peaks that correspond to the core-level photoemission lines of bismuth (Bi) and oxygen (O), thereby demonstrating the successful synthesis of Bi_2O_3 following thermal conversion from the metal-organic framework (MOF) precursor. The most significant peaks relate to the Bi 4f, Bi 4d, Bi 5d, and O 1s orbitals. Subtle characteristics in elevated energy regions correlate with Bi 4d as depicted in (Fig. 3c) and Bi 5d transitions, reinforcing the coherence of the oxide phase. The O 1s signal at around 530 eV as depicted in (Fig. 3d) signifies the existence of lattice oxygen associated with Bi atoms, confirming the stoichiometric establishment of Bi-O bonds. The lack of further impurity peaks (including nitrogen, or other metallic species) indicates that the surface of the MOF-derived Bi_2O_3 is chemically clean, devoid of substantial contamination or residual MOF ligands. The pronounced



and distinct Bi and O peaks signify a significant level of surface crystallinity and robust Bi–O bonding, which are essential for the improved electrochemical and catalytic efficacy of the MOF derived Bi_2O_3 . The XPS survey substantiates the effective synthesis of high-purity Bi_2O_3 , characterized by well-defined Bi^{3+} oxidation states and pristine surface chemistry, hence proving the efficacy of the MOF-derived synthesis method [24]. The valence band offset ΔE_v is defined by the equation

$$\Delta E_v = (4f - V_{BM}) + \Delta E_{CL} \quad (1)$$

where ECL represents the energy difference between the Bi 4f core levels in Bi_2O_3 , as determined by XPS spectra for this sample [25].

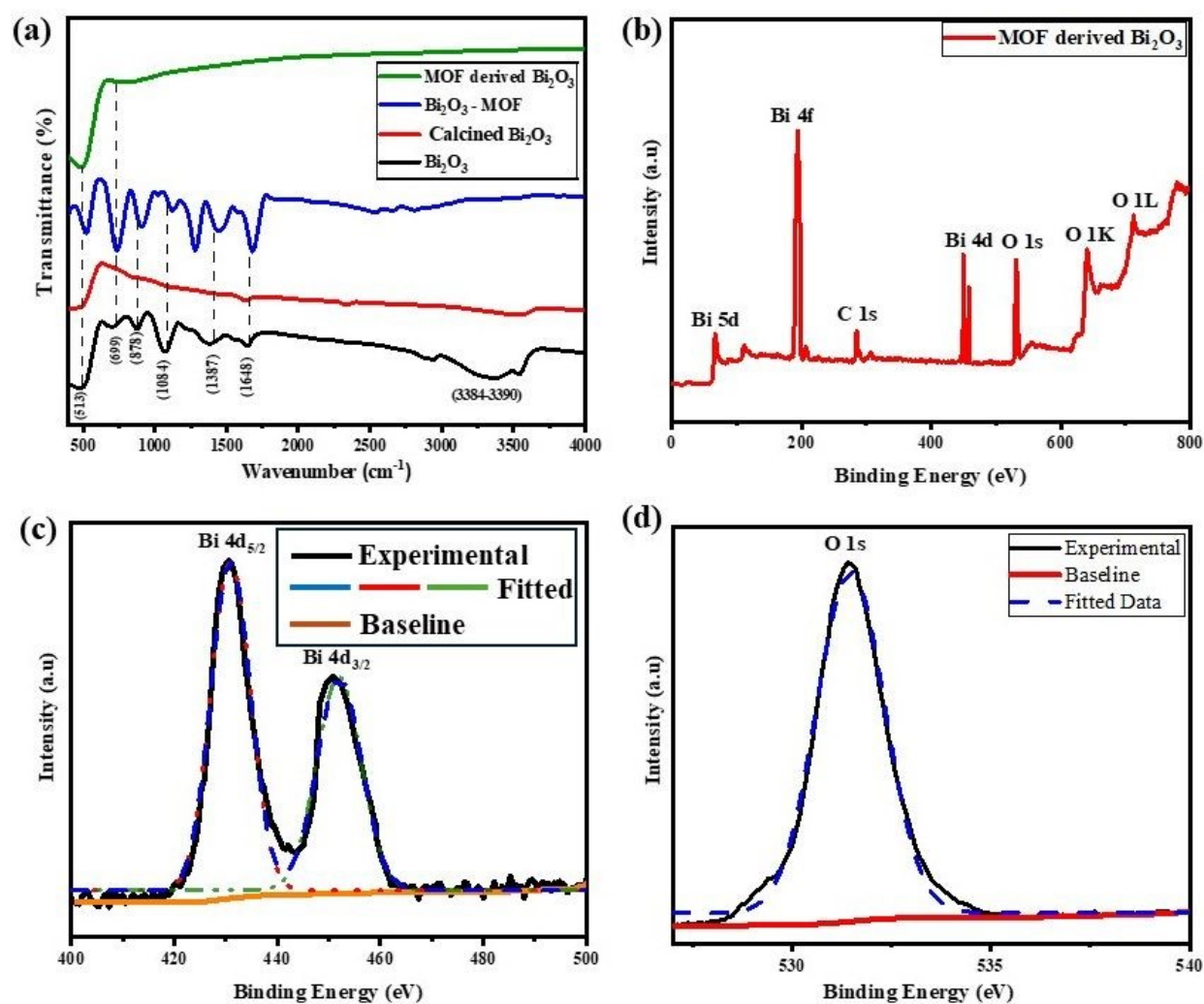
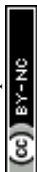


Fig. 3 (a) Fourier transform infra-red Spectroscopy of Bi_2O_3 and MOF derivatives, (b) XPS survey spectrum of MOF-derived Bi_2O_3 , (c) XPS spectrum of Bi 4d bands and (d) Oxygen (O 1s) band in MOF-derived Bi_2O_3 .



The surface morphologies of the synthesized samples were examined using scanning electron microscopy (SEM), as shown in (Fig. 4). The pristine Bi_2O_3 sample exhibits a two-dimensional sheet-like morphology (Fig. 4a, b). The lateral dimensions of the nanosheets are difficult to determine precisely due to slight agglomeration among adjacent sheets [26]. The surfaces appear relatively rough and textured, which may be attributed to residual surface species or nanoscale structural irregularities commonly observed in hydrothermally synthesized metal oxides. In contrast, the calcined Bi_2O_3 sample (Fig. 4c, d) displays a more homogeneous and less distinct sheet-like morphology. The nanosheets appear partially fused, suggesting that sintering occurred during the 500 °C calcination process, leading to the formation of larger agglomerated structures [27]. The smoother surface texture observed after calcination is likely due to the removal of residual surface species and structural rearrangement induced by thermal treatment [27]. The Bi_2O_3 -MOF (Fig. 4e, f) exhibits an irregular and aggregated morphology composed of interconnected nanosheets and particle-like structures [28]. The clustering behavior may be associated with coordination-driven assembly and the bridging effect of organic terephthalate linkers within the framework, resulting in a complex hybrid architecture. Notably, the morphology of the MOF-derived Bi_2O_3 (Fig. 4g, h) is distinctly different from the other samples. It consists of uniformly distributed short rod-like or quasi-spherical nanostructures with visible interparticle voids, indicating the development of a porous architecture. This morphological transformation is attributed to the controlled solvothermal synthesis at 150 °C, followed by thermal decomposition of the MOF precursor at 500 °C, which facilitates structural reconstruction and pore formation [29, 30]. The resulting hierarchical structure is expected to enhance electrolyte accessibility and ion transport during electrochemical operation.



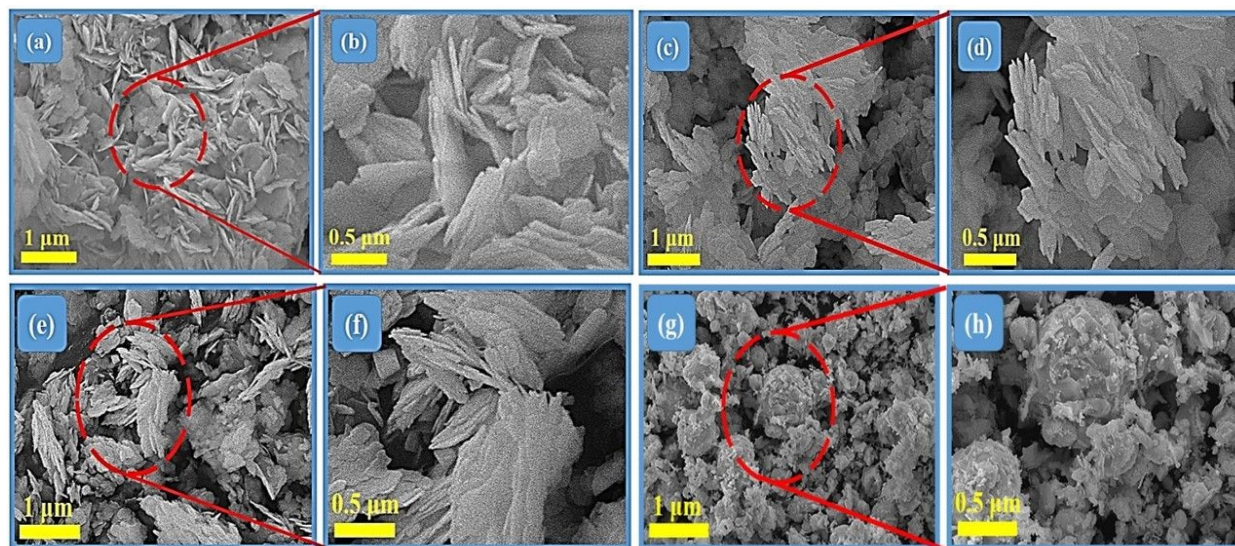


Fig. 4 (a, b) Low and high-resolution scanning electron microscopy (SEM) images of Bi_2O_3 , (c, d) Calcined Bi_2O_3 , (e, f) Bi_2O_3 -MOF and (g, h) MOF derived Bi_2O_3 .

The elemental compositions of the synthesized samples were examined using energy-dispersive X-ray spectroscopy (EDS), and the corresponding spectra are presented in Fig. 5. The EDS results confirm that pristine Bi_2O_3 , calcined Bi_2O_3 , and MOF-derived Bi_2O_3 are composed exclusively of Bi and O elements, with no detectable impurity peaks, indicating the high purity of the synthesized nanostructures (Fig. 5a, b, and d) [31]. In contrast, the Bi_2O_3 -MOF precursor exhibits additional carbon signals in both the EDS spectra and elemental mapping (Fig. 5c), which originate from the terephthalic acid (TPA) organic linker present in the coordination framework. This observation is consistent with the XRD results confirming the presence of the organic phase prior to calcination [32]. A gradual decrease in the relative oxygen signal intensity is observed after calcination and MOF integration. This change can be attributed to several factors associated with thermal treatment. During calcination at elevated temperatures, physically adsorbed water, hydroxyl groups, and organic linker components decompose and are released as volatile species such as H_2O and CO_2 , thereby reducing the overall oxygen contribution detected by surface-sensitive EDS measurements [33]. Additionally, structural densification and partial pore collapse during thermal treatment may limit oxygen detection from deeper regions due to the limited penetration depth of the EDS technique. The combined effects of dehydration, ligand decomposition, and structural reorganization during calcination contribute to the observed variation in oxygen intensity. Overall, the EDS analysis corroborates the successful formation of high-purity MOF-derived Bi_2O_3 and supports the structural evolution inferred from XRD and FT-IR results [34].



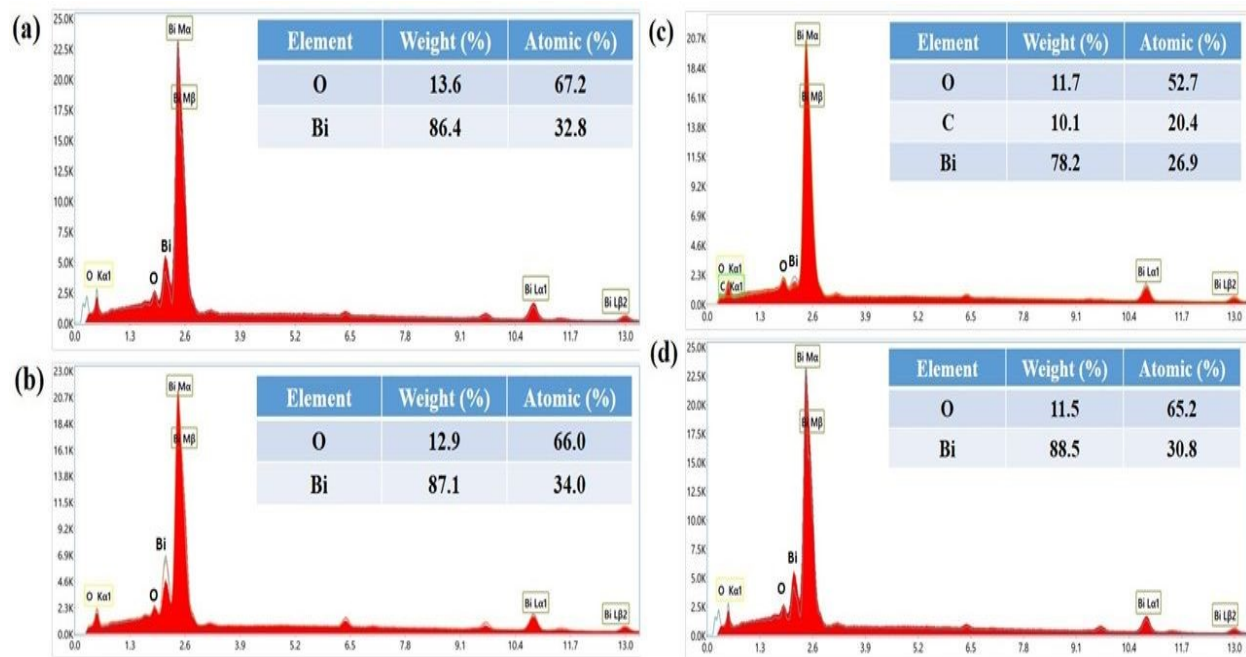


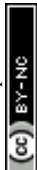
Fig. 5 Energy dispersive x-ray spectroscopy (EDS) spectra of (a) Bi_2O_3 , (b) Calcined Bi_2O_3 (c) Bi_2O_3 -MOF and (d) MOF derived Bi_2O_3 .

Electrochemical Analysis

To demonstrate the electrochemical analysis, cyclic voltammetry (CV) analysis was carried out for synthesized samples performed at scan rates from (5 to 100 mV s^{-1}) within a potential window of (0 to 0.6 V) as shown in (Fig. 6a-d), demonstrates pseudo-capacitive behavior, with clear oxidation and reduction peaks at both ends of the scan, resulting in a duck-shaped curve. As the scan rate increases, the active area beneath the CV curves broadens due to a heightened current response. However, the charge storage capacity diminishes with faster scan rates, which restrict ion diffusion into the deeper active sites of the electrode, making the process more dominated by surface interactions. The redox peaks identified in the CV curves indicate the reversible transformation between ($\text{Bi}^{3+}/\text{Bi}^{5+}$) [44], represented by the reaction:



This emphasizes the Faradaic charge storage mechanism. The characteristic duck-like shape of the CV curves further supports the coexistence of capacitive and diffusion-controlled processes, typical of pseudo-capacitive materials. The oxidation peak (anodic) indicates the formation of BiOOH , while the reduction peak (cathodic) represents the return to Bi_2O_3 , demonstrating a



complete reversible electrochemical redox reaction at the electrode/electrolyte interface. This behavior underscores the potential of Bi_2O_3 as an electrode material in electrochemical energy storage devices, where the interplay between rapid surface reactions and bulk redox activity dictates its electrochemical performance [12]. These redox reactions at the electrode-electrolyte interface account for the observed super-capacitive behavior. Among the synthesized samples, the MOF-derived Bi_2O_3 demonstrates the highest charge storage capacity, with a high current value due to its extensive specific surface area resulting from its ultra-microporous structure, as shown in (Fig. 6d). This facilitates greater involvement in electrochemical reactions, the integration of MOFs with Bi_2O_3 leads to an ultra-micropores, mesopores, and macropores structure that enhances the surface-to-volume ratio, resulting in a nanoscale morphology defined by nanoporous and agglomerated structures. This configuration improves ion diffusion efficiency and allows adequate time for electrolyte ions to undergo the electrochemical redox reaction at the surface, thus optimizing electrochemical performance [45].

Furthermore, to gain a deeper understanding of the electrochemical reaction kinetics associated with Bi_2O_3 and its MOF derivatives, Randles-Sevcik correlations were conducted, as depicted in (Fig. 6e-h). The Randles-Sevcik equation (equation 4 Supplementary information) was employed to analyze the electrochemical behavior of various Bi_2O_3 samples by correlating their peak currents with scan rates in CV measurements conducted within the (0-0.6 V) potential window. The synthesized Bi_2O_3 exhibited decreasing electrochemical performance compared to MOF-derived Bi_2O_3 , with a sublinear correlation between peak current and scan rate, suggesting restricted charge transfer due to factors such as grain boundary resistance, defect ordering, or limited electronic conductivity. In contrast, calcined Bi_2O_3 displayed a weak peak current, attributed to insulating grain boundaries and reduced active surface area caused by particle agglomeration during high-temperature treatment [46]. The Bi_2O_3 -MOF demonstrated significantly moderate peak currents, in comparison with calcined Bi_2O_3 owing to its high surface area and porous framework, which facilitated efficient ion diffusion and rapid redox kinetics. The best performance was observed in the fully porous MOF-derived Bi_2O_3 , which exhibited the highest peak current due to its interconnected conductive pathways, maximized electrode-electrolyte contact area, and minimal diffusion barriers, optimizing charge storage and electron transfer kinetics [47].

The correlation coefficients (R^2) are derived from the linear fit applied on peak current versus scan rate in Randles-Sevcik plots, as presented in (Table 2).



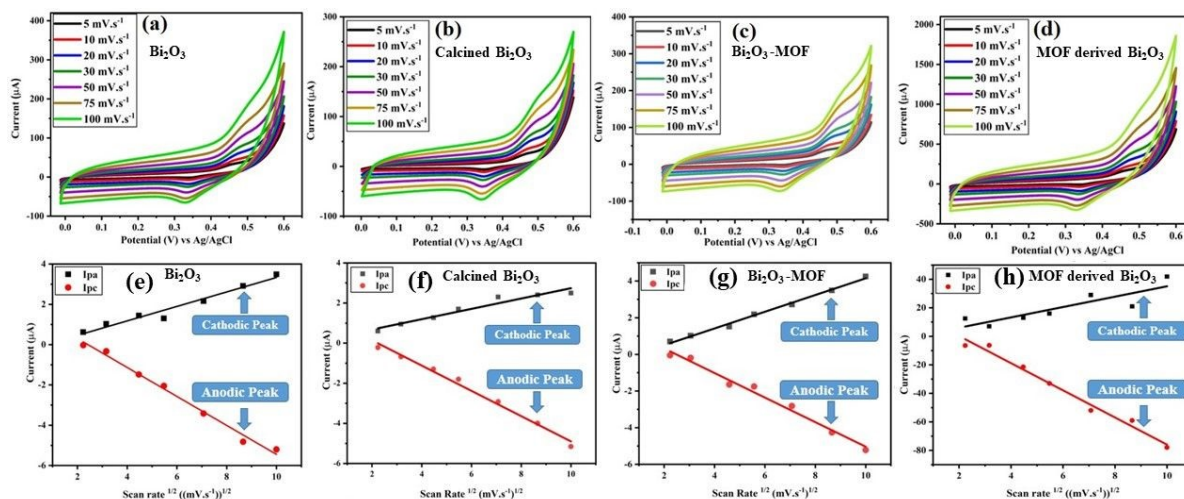


Fig. 6 Cyclic voltammetry curves of (a) Bi_2O_3 (b) Calcined Bi_2O_3 (c) Bi_2O_3 -MOF, (d) MOF derived Bi_2O_3 within (0-0.6) potential window: Randle-Sevcik correlations of (e) Bi_2O_3 , (f) calcined Bi_2O_3 , (g) Bi_2O_3 -MOF and (h) MOF derived Bi_2O_3 .

Capacitive limited and diffusion limited regions were analyzed using CV for both Bi_2O_3 and MOF-derived Bi_2O_3 samples as depicted in (Fig. 7), to comprehend the detailed electrochemical activity at the electrode/electrolyte interface within three-electrode configurations. The regions were analyzed using a linear fit on the cathodic peak observed in the CV curves, employing Dunn's model to differentiate between the diffusion and capacitive regions within the CV curves. (Fig. 7a-f) illustrates the cathodic peak fit, capacitive and diffusion regions, along with a bar representation of these regions for Bi_2O_3 and MOF derived Bi_2O_3 . The distinct redox peaks indicate a battery-type, Faradaic charge storage mechanism driven by reversible chemical reactions. The primary diagnostic method involves constructing log (peak current) versus log (scan rate) plots. The slope of the linear fit provides a critical b-value, which indicates the charge storage mechanism. The calculated b-values were 0.2 for pristine Bi_2O_3 and 0.5 for MOF-derived Bi_2O_3 . A b-value close to 0.5 suggests a diffusion-controlled charge storage mechanism, whereas values approaching 1.0 indicate surface-controlled capacitive behavior. The relatively low b-value (0.2) for pristine Bi_2O_3 indicates a dominant diffusion-controlled limitation. In contrast, the MOF-derived Bi_2O_3 exhibits a b-value of 0.5, suggesting improved charge transfer kinetics and reduced diffusion constraints compared to pristine Bi_2O_3 , although the process remains primarily diffusion-controlled [13-16, 35].

The observed increase indicates that the distinctive ultra-micropores, mesopores, and macropores structure derived from the MOF precursor significantly improves kinetics by



promoting a larger capacitive contribution, suggesting accelerated ion transport and enhanced charge storage at the electrode-electrolyte interface. The figure demonstrates that nanostructuring through MOF derivation effectively alters the material electrochemical profile, resulting in a hybrid electrode with enhanced battery-like capacity and capacitor like rate capability, which is advantageous for high-performance energy storage devices [36].

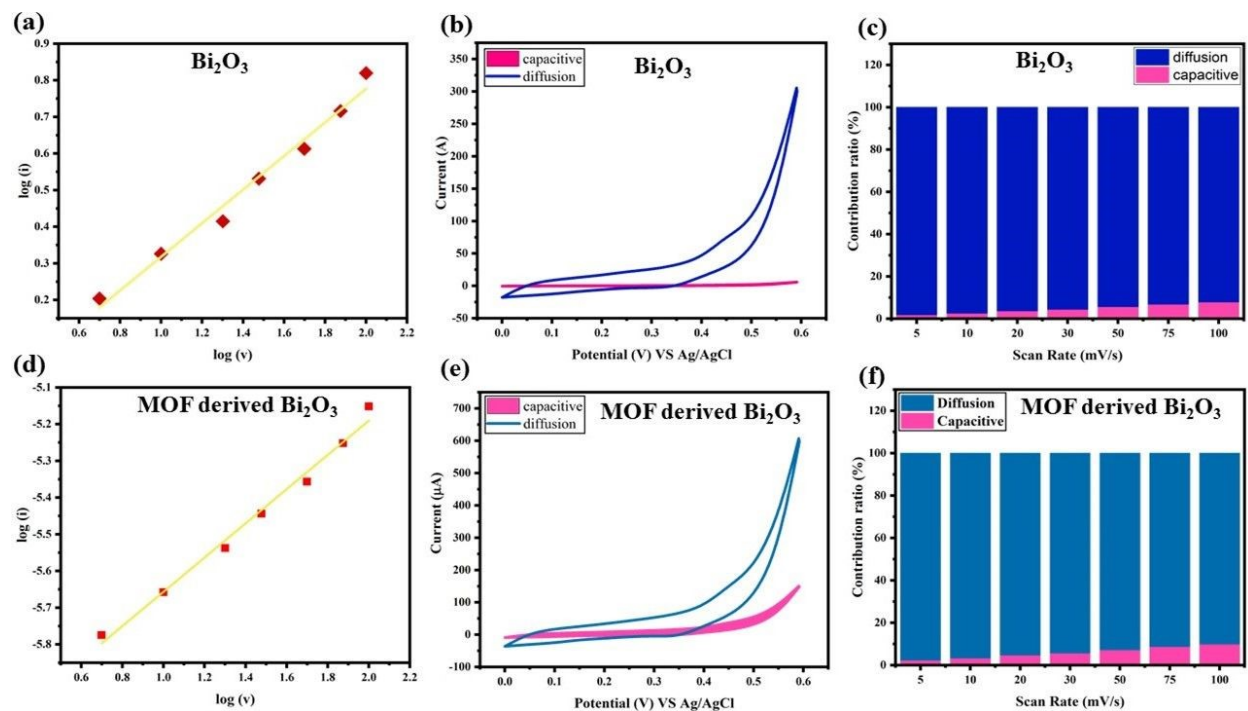


Fig. 7 (a) Cathodic peak fit, (b) Capacitive and diffusion regions, (c) scan rate vs distribution (%) of Bi_2O_3 , (d) Cathodic peak fit, (e) Capacitive and diffusion regions, (f) scan rate vs distribution (%) of MOF-derived Bi_2O_3 .

To study the electrochemical kinetics at the electrode/electrolyte interface, the electrochemical impedance spectroscopy (EIS) technique was used, and (Fig. 8a) shows the Nyquist plots of the prepared samples and the equivalent circuit diagram. The spectra observed were successfully modeled by an equivalent circuit that included solution resistance (R_s), constant phase element (CPE), charge transfer resistance (R_{ct}) and Warburg impedance (W), as shown as an inset of (Fig. 8a). The high-frequency intercept in the Nyquist representation is proportional to the value of R_s , which had a zero impact in the comparative analysis, whereas the semicircular diameter in the medium-frequency band directly relates to the value of the R_{ct} , the kinetics of charge transfer across the electrode/electrolyte interface [37]. The element of the Warburg that is found in the low frequencies area in the electrode structure reflects the finite diffusion of ions in the electrode structure. The trends of the R_{ct} values as shown in (Table 3) are as follows: calcined



Bi_2O_3 has the highest Rct of 655 Ω , then pristine Bi_2O_3 with Rct of 523 Ω and Bi_2O_3 -MOF 573 Ω , and MOF-derived Bi_2O_3 with Rct of 345 Ω . The progressive decrease in Rct indicates improved interfacial charge-transfer kinetics based on its wide ultra-micropores, mesopores, and macropores structure and optimal specific surface area, which sum up to provide numerous electroactive sites of the fast redox reaction [38].

To extend the electrochemical kinetics analysis, the Bode plots also give more information about the impedance behavior at different frequencies, and can be seen to follow a systematic trend that is highly correlated with the values of Rct (Fig. S1 Supplementary information). The impedance modulus $|Z|$ in the low-frequency region (10^{-1} to 10^{-2} Hz) of the Bode magnitude plot is mostly the total cell resistance of the combination of the R_s and Rct, and the high-frequency plateau (10^{-4} to 10^{-5} Hz) corresponds to mostly the uncompensated solution resistance. In line with the trend of Rct, the sample of calcined Bi_2O_3 with the highest Rct of 655 Ω has the highest possible $|Z|$ throughout the frequency range, indicating significantly sluggish charge transfer rate constants with a low intrinsic conductivity and low electroactive surface area. Continuing with the trend, the pure Bi_2O_3 sample would have intermediate values of the $|Z|$ in the range of the values of Z that relate to moderate Rct of 523 Ω that the metal-organic framework does not offer efficient charge carrier motion [38]. The lowest Rct of 345 Ω MOF-derived Bi_2O_3 is most prominently observed as a sharp fall in $|Z|$ within mid-to-high frequencies and a pronounced phase angle maximum peak occurring at the higher frequencies. This time-dependent variation is indicative of elevated charge transfer kinetics, in which the time constant of relaxation reduces significantly, and the electrode surface is capable of faster faradaic processes.

This increase in the progressive trend is further supported by the phase angle plots: materials with high Rct such as calcined Bi_2O_3 exhibit larger and more pronounced phase angle peaks which are evidence of more resistive capacitive behavior and slower electrode kinetics. Also, as the Rct decreases over the series, the phase angle response gets narrower and narrower, with the MOF-derived Bi_2O_3 having the most narrowed phase angle response indicating transition to resistive-dominated behavior at higher frequencies because the electron transport is facilitated and interfacial charge buildup is reduced. This negative relationship between falling Rct values and the overall systematic decrease in impedance modulus throughout the Bode plots proves that the synthetic pathway utilizing MOF has been effective in fabricating Bi_2O_3 with a favorable microstructure. The increased porosity, increased specific surface area and better electrical



connectivity all reduce the activation energy size of charge transfer and consequently increase the rate of electrochemical reactions, thus making the MOF-derived Bi_2O_3 the better electrode substance between the samples that were synthesized [37].

To examine the charge discharge behavior of Bi_2O_3 and its MOF derivatives, galvanostatic charge discharge (GCD) tests were conducted under different current densities of 0.5 to 10 A g^{-1} (Fig. 8b-e). Charge discharge profiles of all samples are relatively symmetric which means that electrochemical reversibility of the process is good and the charge storage characteristics of the samples are stable. Both the discharge time varies with current density and at a given current density, the higher the current density the lower the discharge time, leading to a smooth decline in specific capacitance as shown in the (Fig. 8f). The trend is in line with the negative dependence between current density and discharge time (Equation 3, Supplementary Information). The quasi-triangular but a little nonlinear GCD profiles imply that both the electric double-layer capacitance (EDLC) and Faradaic redox processes coexist. The deviation of an ideal linear triangular shape proves the role of pseudocapacitive behavior related to reversible $\text{Bi}^{3+}/\text{Bi}^{5+}$ redox transitions in alkaline electrolyte.

The MOF-derived Bi_2O_3 electrode has the largest specific capacitance and has a capacitance of 876 F g^{-1} at 0.5 A g^{-1} as indicated in (Table 2). Such high performance is credited to its ultra-microporous structure that it inherits the MOF building block. The porous system minimizes ion diffusion distances and enhances the speed of charge transfers and increases the electrochemically active surface area. Moreover, the hierarchical pore structure promotes effective penetration of the electrolytes, and the effective utilization of the redox-active sites in Bi position. Conversely, pure Bi_2O_3 , calcined Bi_2O_3 and Bi_2O_3 -MOF composites have relatively lower values of capacitance, which may be explained through less easy accessibility to the surface and less optimized architecture of pores. The capacitance values of all samples decrease in a progressive manner as the current density increases indicating characteristic rate-related restrictions of ion diffusion. The measured electrochemical character can be seen to indicate that the structural engineering through MOF templating strongly increases ion transport routes, redox access, and total charge storage ability. The additive value of the electric double-layers and reversible Faradaic reactions leads to enhanced capacitance and rate capability of the MOF-derived Bi_2O_3 electrode.

The results of the detailed capacitance at various current densities are summarized in (Table 2).



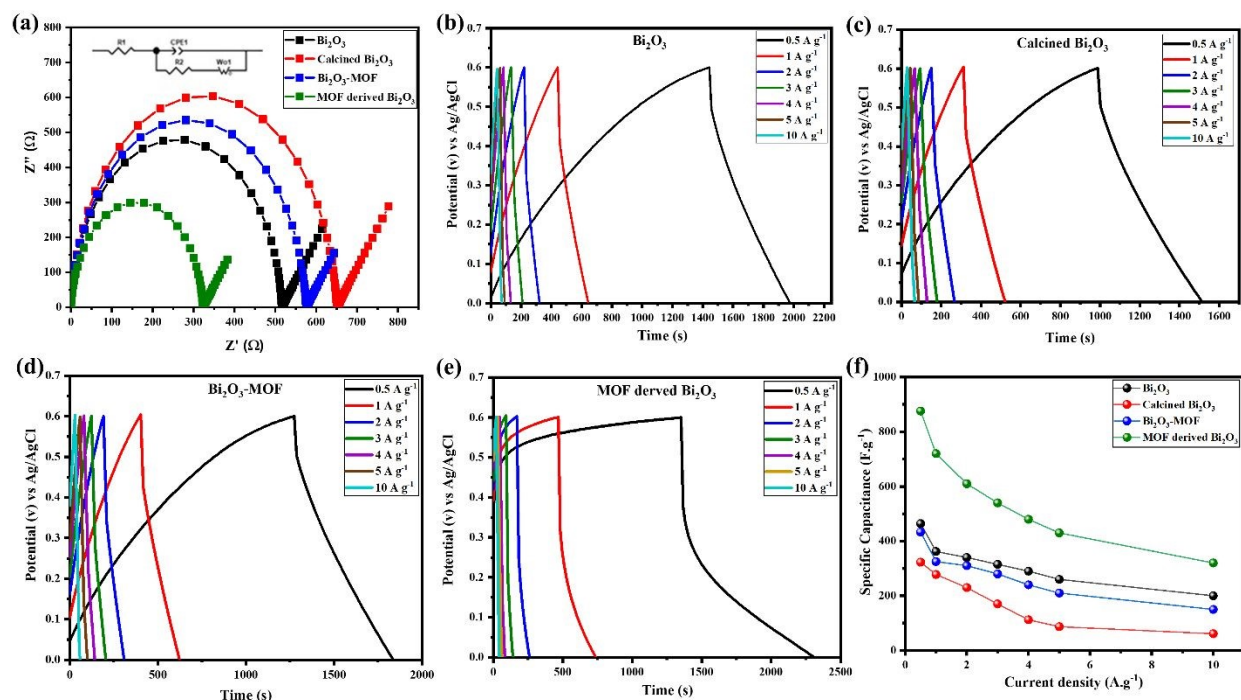


Fig. 8 (a) EIS Nyquist spectra (b) Galvanostatic charge/discharge curves of Bi_2O_3 (c) Calcined Bi_2O_3 (d) Bi_2O_3 -MOF (e) MOF derived Bi_2O_3 (f) Current density (A.g^{-1}) vs specific capacitance (F.g^{-1}).

Table 2: Specific capacitance vs current densities, charge transfer resistance and Correlation factor (R^2) of Bi_2O_3 , Calcined Bi_2O_3 , Bi_2O_3 -MOF and MOF derived Bi_2O_3 .

S. No	Sample	Current density (A.g^{-1})	Specific capacitance (F.g^{-1})	Rct (Ω)	Correlation Factor
1	Bi_2O_3	0.5	464	523	0.92
		1	362		
		2	340		
		3	315		
		4	290		
		5	260		
		10	200		
		0.5	323		
		1	278		
		2	230		
2	Calcined Bi_2O_3	3	170	655	0.83
		4	112		
		5	87		
		10	61		
		0.5	433		
		1	325		
3	Bi_2O_3 -MOF	2	310	573	0.87
		3	280		
		4	240		
		5	210		
		10	150		
		0.5	876		
4	MOF derived Bi_2O_3	1	720	345	0.98
		2	610		
		3	540		
		4	480		
		5	430		



10

320

Symmetric Device Configuration

For practical validation of electrochemical stability and structural durability, a symmetric supercapacitor device was assembled using MOF-derived Bi_2O_3 as both the positive and negative electrodes, as illustrated in (Fig. 9a). The cyclic voltammetry (CV) profiles of the fabricated symmetric device are presented in (Fig. 9b), recorded at scan rates of 10, 20, 30, 50, 75, and 100 mV s^{-1} within a potential window of 0–0.6 V. When the operating voltage was extended beyond 0.6 V, noticeable distortion in the CV and GCD profiles was observed, accompanied by increased polarization and a decline in coulombic efficiency. These changes indicate the onset of parasitic water-splitting reactions, including oxygen evolution (OER) and hydrogen evolution (HER), under alkaline conditions. Therefore, 0–0.6 V was selected as the optimal and stable operating window to ensure reversible charge storage and suppress undesired side reactions. With increasing scan rate, the enclosed area of the CV curves gradually decreases, reflecting reduced charge storage capability at higher scan rates. This behavior is attributed to kinetic limitations, where rapid potential sweeping restricts electrolyte ion diffusion into deeper active sites, leading to partial utilization of the electrochemically active surface. The symmetric MOF-derived Bi_2O_3 device exhibits distinct anodic and cathodic peaks, characteristic of faradaic redox processes associated with the reversible $\text{Bi}^{3+}/\text{Bi}^{5+}$ transformation in alkaline electrolyte [36]. The quasi-rectangular yet redox-featured CV profiles confirm the pseudocapacitive nature of the charge storage mechanism. The observed behavior suggests that the energy storage process involves a synergistic contribution from surface-controlled redox reactions and diffusion-assisted ion transport within the hierarchical porous structure of the electrode material.

(Fig. 9c) presents the Nyquist plot of the symmetric MOF-derived Bi_2O_3 device along with the corresponding equivalent circuit model employed to fit the impedance data. The equivalent circuit consists of the solution resistance (R_s), a constant phase element (CPE), charge-transfer resistance (R_{ct}), Warburg impedance (W), and a capacitive element (C). In the high-frequency region, the intercept on the real axis represents the solution resistance (R_s), which arises from the intrinsic resistance of the electrolyte, current collectors, and electrical contacts. The semicircular arc observed in the intermediate frequency region corresponds to the charge-transfer resistance (R_{ct}) at the electrode/electrolyte interface, reflecting the kinetics of faradaic reactions. In the low-frequency region, the inclined linear tail is attributed to the



Warburg impedance, indicating diffusion-controlled ion transport within the porous electrode structure. The symmetric MOF-derived Bi_2O_3 device exhibits an R_{ct} value of 433Ω (Table 3). Although the absolute R_{ct} appears relatively high compared to highly conductive carbon-based electrodes, this is primarily attributed to the intrinsic semiconducting nature of Bi_2O_3 , which possesses lower electronic conductivity. Furthermore, impedance measurements performed in a symmetric two-electrode configuration inherently include the combined interfacial resistances of both electrodes, the separator, and electrolyte contributions, resulting in higher apparent resistance values. Importantly, the comparative analysis among the synthesized samples reveals a systematic decrease in R_{ct} for the MOF-derived Bi_2O_3 , indicating improved charge-transfer kinetics. The reduced semicircle diameter and lower diffusion impedance suggest enhanced ion transport and interfacial electrochemical activity. This improvement is attributed to the hierarchical porous architecture and increased electrochemically active surface area of the MOF-derived Bi_2O_3 , which facilitate efficient electrolyte penetration and accelerate faradaic redox reactions at the electrode/electrolyte interface [39].

Galvanostatic charge/discharge (GCD) measurements were performed to evaluate the charge storage behavior and electrochemical performance of the fabricated symmetric MOF-derived Bi_2O_3 device. The GCD profiles were recorded at various current densities to assess rate capability and charge/discharge characteristics (Fig. 9d). The curves exhibit a nearly symmetric triangular shape with slight deviations, indicating predominantly pseudocapacitive behavior with minor resistive contributions. At a current density of 0.5 A g^{-1} , the symmetric device demonstrated an extended discharge time, corresponding to a high specific capacitance of 950 F g^{-1} . Based on this value and an operating voltage window of 0.6 V , the device achieved a maximum energy density of 47.2 Wh kg^{-1} with a corresponding power density of 150 W kg^{-1} , as summarized in (Table 3). With increasing current density, the specific capacitance gradually decreased to 358 F g^{-1} at 10 A g^{-1} , while the power density increased to 3000 W kg^{-1} , demonstrating good rate capability. The enhanced electrochemical performance is attributed to the synergistic effect of the faradaic redox activity of Bi_2O_3 and the hierarchical porous structure derived from the MOF precursor. The multiscale pore network provides abundant electroactive sites and facilitates efficient ion transport, thereby improving charge storage efficiency and power performance. These results demonstrate that MOF-derived Bi_2O_3 is a promising electrode material for high-performance pseudocapacitor applications.



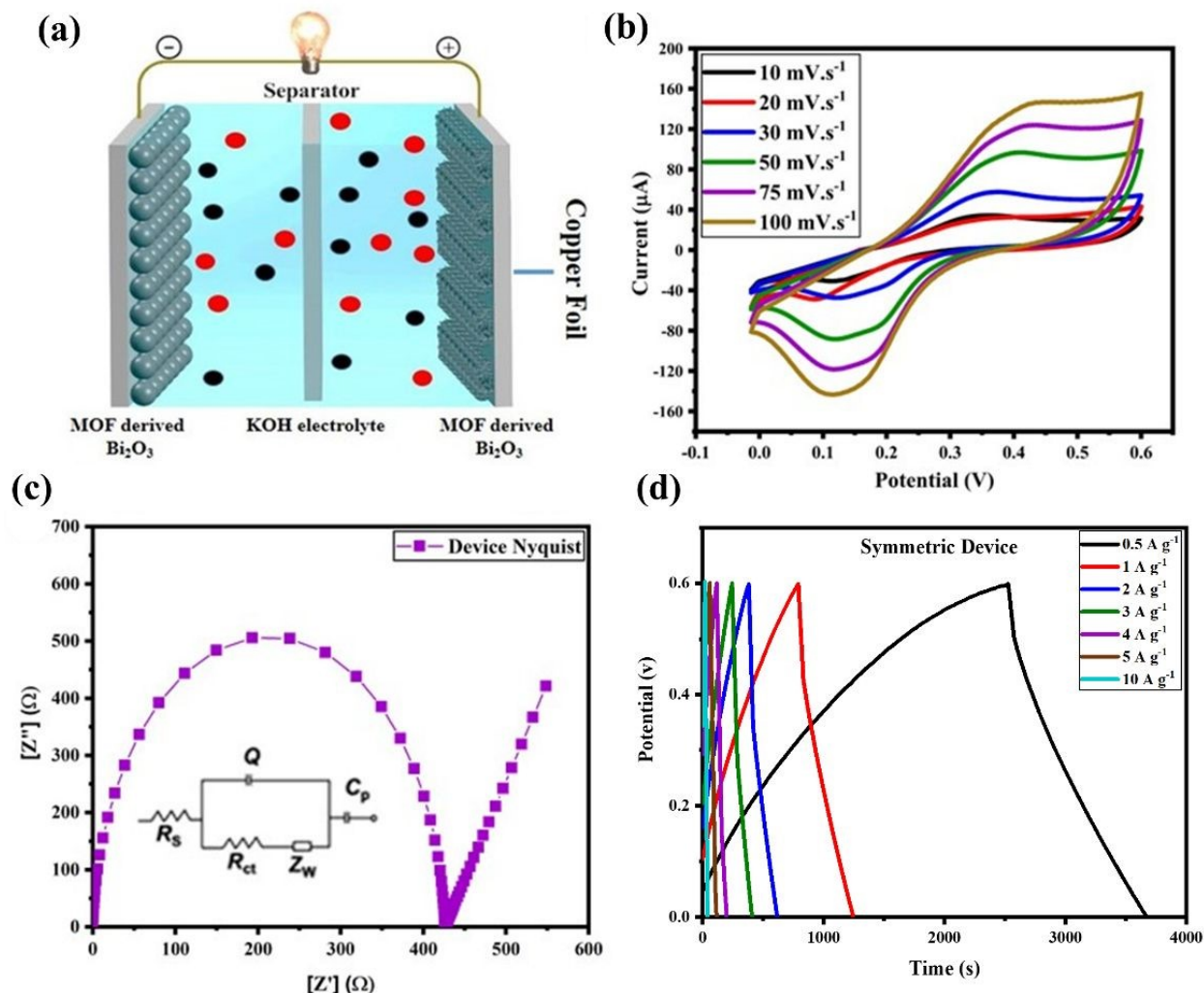
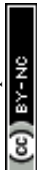


Fig. 9 (a) fabricated symmetric device schematic (b) Cyclic voltammetry (CV) curves (c) EIS Nyquist fitted spectra with equivalent fitting circuit and (d) Galvanostatic charge/discharge GCD curves.

The electrochemical stability of the fabricated symmetric supercapacitor was evaluated through 10,000 continuous galvanostatic charge–discharge (GCD) cycles, as shown in Fig. 10. The device retained 75.3% of its initial capacitance after 10,000 cycles, with a Coulombic efficiency of 81.4% (Table 3), demonstrating acceptable long-term stability for a metal oxide-based pseudocapacitor. The observed stability is attributed to the hierarchical porous architecture inherited from the MOF precursor, which promotes efficient electrolyte diffusion, minimizes polarization effects, and alleviates structural stress during repeated charge–discharge cycling. The synergistic contribution of electric double-layer capacitance and reversible faradaic redox reactions further supports sustained charge storage performance. The interconnected ultramicroporous and mesoporous framework enhances ion–electrode interactions while



maintaining structural integrity, thereby contributing to stable electrochemical behavior over prolonged cycling [40].

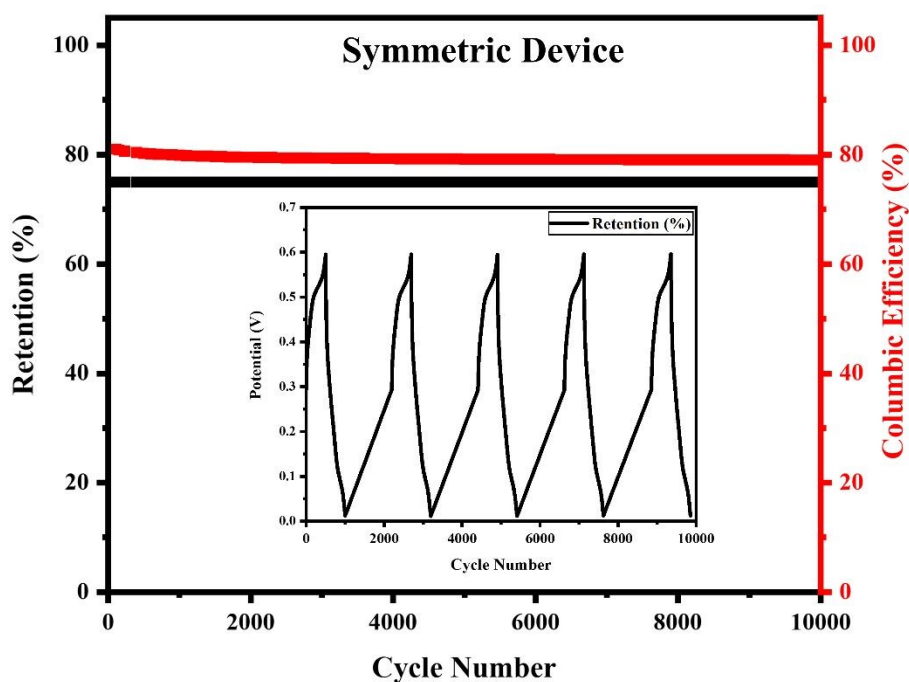


Fig. 10 Cyclic Stability Retention (%) and Coulombic efficiency (%) of fabricated symmetric device over 10,000 cycles.

Table 3: Cs, Energy density, power density, Diffusion co-efficient, Rct, and Cyclic Stability Retention (%) and Coulombic efficiency (%) of the fabricated Symmetric MOF derived Bi₂O₃ supercapacitor device.

Device	Current density (A.g ⁻¹)	Specific Capacitance (F g ⁻¹)	Energy density (Wh Kg ⁻¹)	Power density (W Kg ⁻¹)	Diffusion co-efficient (cm ² /s)	Rct (Ω)	Retention (%)	Coulombic efficiency (%)
Symmetric Device	0.5	950	47.2	150	3.8×10^{-12}	433	75.3%	81.4%
	1	720	39	300				
	2	618	36	600				
	3	590	31	900				
	4	517	25	1200				
	5	478	21	1500				
	10	358	18	3000				

The performance of the MOF-derived Bi₂O₃ symmetric device is benchmarked against other Bi₂O₃-based supercapacitors in the Ragone plot shown in (Fig. 11). This plot clearly illustrates the device's competitive performance, navigating the classic trade-off where increasing power density leads to a decrease in achievable energy density.



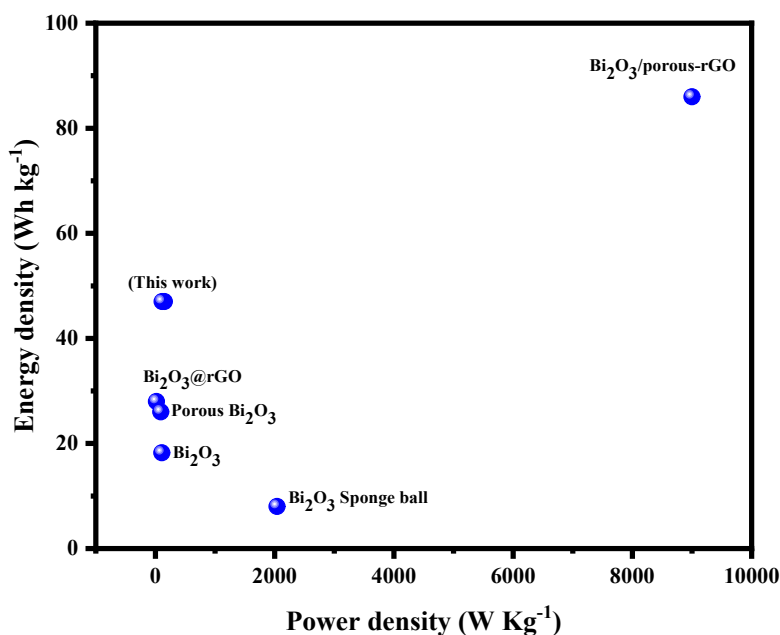


Fig. 11 Ragone plot illustrating the relationship between energy density and power density of the fabricated MOF-derived Bi₂O₃ symmetric supercapacitor device, compared with previously reported Bi₂O₃-based electrodes in aqueous electrolytes [41-45].

Conclusion

This study systematically investigated the electrochemical performance of bismuth oxide (Bi₂O₃) and MOF-derived Bi₂O₃ nanoporous frameworks as electrode materials for supercapacitor applications. The materials were successfully synthesized via a solvothermal-calcination strategy and comprehensively characterized using X-ray diffraction (XRD), Brunauer–Emmett–Teller (BET) analysis, X-ray photoelectron spectroscopy (XPS), Fourier transform infrared spectroscopy (FT-IR), scanning electron microscopy (SEM), and energy-dispersive X-ray spectroscopy (EDX).

XRD analysis confirmed the formation of δ -Bi₂O₃, while the MOF precursor exhibited additional diffraction peaks corresponding to the terephthalate (TPA) organic linker, consistent with FT-IR results. BET measurements revealed surface areas of 19, 15, 58, and 117 m² g⁻¹ for Bi₂O₃, calcined Bi₂O₃, Bi₂O₃–MOF, and MOF-derived Bi₂O₃, respectively. The MOF-derived Bi₂O₃ exhibited a hybrid Type I/Type IV isotherm with a pronounced hysteresis loop, indicating a hierarchical pore structure composed of dominant ultramicropores (0.42 nm), mesopores, and macropores. XPS analysis confirmed the presence of Bi³⁺ and lattice oxygen species with well-



defined Bi–O bonding, while SEM observations demonstrated a morphological evolution from nanosheets to uniformly distributed porous rod-like nanostructures after MOF-derived transformation.

Electrochemical evaluation in a three-electrode configuration revealed an inverse relationship between specific capacitance (C_{sp}) and charge-transfer resistance (R_{ct}). The MOF-derived Bi_2O_3 achieved a high specific capacitance of 876 F g^{-1} at 0.5 A g^{-1} with a reduced R_{ct} of 345Ω , attributed to its enlarged surface area and hierarchical porous architecture that enhances ion accessibility and redox utilization. When assembled into a symmetric device operating within a $0\text{--}0.6 \text{ V}$ window, the electrode delivered a device-specific capacitance of 950 F g^{-1} at 0.5 A g^{-1} , an energy density of 47.2 Wh kg^{-1} , and a power density of 150 W kg^{-1} . The device retained 75.3% of its initial capacitance after 10,000 cycles, with a Coulombic efficiency of 81.4%, demonstrating acceptable long-term stability.

Overall, the results confirm that MOF-assisted structural engineering effectively enhances pore architecture, ion transport pathways, and electroactive surface utilization in Bi_2O_3 -based electrodes. This strategy provides a viable route for improving the electrochemical performance of metal oxide materials in advanced supercapacitor applications.

Author Contributions

Maaz Khan: Methodology, Investigation, Formal Analysis, Writing-Original Draft. **Adil Alshoiabi:** Software. **Atizaz Ali:** Validation, Investigation, Data Curation. **Qi Liu:** Conceptualization, Resources, Writing-Review & Editing, Supervision, Project Administration. **Syeda Khalida:** Formal Analysis. **Maria Nazir:** Resources, Software. **Baseena Sardar:** Investigation, Data Curation. **Majid Khan:** Conceptualization, Resources, Writing-Review & Editing, Supervision, Project Administration.

All authors reviewed the manuscript.

Declaration of Competing Interest

The authors assert that there are no known conflicting financial interests or personal ties that may have influenced the material presented in this publication.

Data availability

Data will be provided upon request.

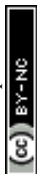


Acknowledgments

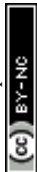
The authors thank the Energy Research Laboratory (ERL) Department of Physics, Abdul Wali Khan University 23200 Mardan and China University of Mining and Technology Xuzhou, China” for Characterization support. This work was also supported by the National Natural Science Foundation of China (Grant Nos. 52272187), the Natural Science Foundation of Inner Mongolia Autonomous Region of China (2024ZD11). This work was supported by the Deanship of Scientific Research, Vice Presidency for Graduate Studies and Scientific Research, King Faisal University, Saudi Arabia [Grant No. KFU254806].

References

- [1] Simon, P., and Gogotsi, Y, *Nature materials*, 2008, 7, 845-854, DOI: 10.1038/nmat2297.
- [2] Khan, M. M., Zhao, Y., Liu, Q., He, W., Mu, D., Li, L., and Wu, F, *Journal of Energy Storage*, 2025, 116, 116038, DOI: 10.1016/j.est.2025.116038.
- [3] Xiao, Q., Zhu, J., Cheng, C., Liu, J., Zhang, X., Li, Z., and Zhu, J, *Nanoscale*, 2023, 15, 3884-3892, DOI: 10.1039/D2NR07096K.
- [4] Jiang, N., and Wachsman, E. D, *Journal of the American Ceramic Society*, 1999, 82, 3057-3064, DOI: 10.1111/j.1151-2916.1999.tb02202.x.
- [5] Li, R., Zhang, W., and Zhou, K, *Advanced Materials*, 2018, 30, 1705512, DOI: 10.1002/adma.201705512.
- [6] Kaneti, Y. V., Tang, J., Salunkhe, R. R., Jiang, X., Yu, A., Wu, K. C. W., and Yamauchi, Y, *Advanced materials*, 2017, 29, 1604898, DOI: 10.1002/adma.201604898.
- [7] Wang, Y., Sun, H., Yang, Z., Zhu, Y., and Xia, Y, *Carbon Neutralization*, 2024, 3, 737-767, DOI: 10.1002/cnl2.153.
- [8] Wu, J., Wang, K., Hu, J., Li, J., Wang, K., Wu, J., ... and Zhang, W, *Journal of Energy Storage*, 2024, 102, 114024, DOI: 10.1016/j.est.2024.114024.
- [9] PA, P., and Christopher Selvin, P, *Journal of Solid-State Electrochemistry*, 2025, 29, 4747-4761, DOI: 10.1007/s10008-025-06340-y.



- [10] Wang, L., Han, Y., Feng, X., Zhou, J., Qi, P., and Wang, B, *Coordination Chemistry Reviews*, 2016, 307, 361-381, DOI: 10.1016/j.ccr.2015.09.002.
- [11] Kaduk, J. A, *Journal of research of the National Institute of Standards and Technology*, 1996, 101, 281, DOI: 10.6028/jres.101.029.
- [12] Fruth, V., Ianculescu, A., Berger, D., Preda, S., Voicu, G., Tenea, E., and Popa, M, *Journal of the European Ceramic Society*, 2006, 26, 3011-3016, DOI: 10.1016/j.jeurceramsoc.2006.02.019.
- [13] Kim, M. K., Kim, M. S., Park, J. H., Kim, J., Ahn, C. Y., Jin, A., ... and Sung, Y. E, *Nanoscale*, 2020, 12, 15214-15221, DOI: 10.1039/D0NR03219K.
- [14] Qin, Y., Hu, C., Huang, Q., Lv, Y., Song, Z., Gan, L., and Liu, M, *Nano-micro letters*, 2026, 18, 38, DOI: 10.1007/s40820-025-01883-1.
- [15] Fan, W., Tian, S., Qin, L., Alomar, T. S., Ruan, P., El-Bahy, Z. M., ... and Zhou, J, *Journal of the American Chemical Society*, 2025, 147, 18694-18703, DOI: 10.1021/jacs.5c01648.
- [16] Hossain, M. S., Kabir, M. H., Pabel, M. Y. and Yasmin, S, *Materials Advances*, 2026, DOI: 10.1039/D5MA01144B.
- [17] Phillips, R., Jolley, K., Zhou, Y., and Smith, R, *Carbon Trends*, 2021, 5, 100124, DOI: 10.1016/j.cartre.2021.100124.
- [18] Boi, F. S., Liu, M., Xia, J., Odunmbaku, O., Taallah, A., and Wen, J, *Carbon*, 2019, 150, 27-31, DOI: 10.1016/j.carbon.2019.05.003.
- [19] Ren, J., Ledwaba, M., Musyoka, N. M., Langmi, H. W., Mathe, M., Liao, S., and Pang, W, *Coordination Chemistry Reviews*, 2017, 349, 169-197, DOI: 10.1016/j.ccr.2017.08.017.
- [20] Lei, A., Yang, G., Pan, K., Liu, W., Deng, C., Fang, M., ... and Lai, F, *Journal of Power Sources*, 2025, 625, 235744, DOI: 10.1016/j.jpowsour.2024.235744.
- [21] Ardelean, I., Cora, S., and Rusu, D, *Physica B: Condensed Matter*, 2008, 403, 3682-3685, DOI: 10.1016/j.physb.2008.06.016.
- [22] Wang, Y., Kretschmer, K., Zhang, J., Mondal, A. K., Guo, X., and Wang, G, *RSC advances*, 2016, 6, 57098-57102, DOI: 10.1039/C6RA11809G.
- [23] Juibari, N. M., and Tarighi, S, *Journal of Alloys and Compounds*, 2020, 832, 154837, DOI: 10.1016/j.jallcom.2020.154837.



- [24] Chai, S. Y., Kim, Y. J., Jung, M. H., Chakraborty, A. K., Jung, D., and Lee, W. I, *Journal of Catalysis*, 2009, 262, 144-149, DOI: 10.1016/j.jcat.2008.12.020.
- [25] Drache, M., Roussel, P., and Wignacourt, J. P, *Chemical reviews*, 2007, 107, 80-96, DOI: 10.1021/cr050977s.
- [26] Pooladi, M., and Zerafat, M. M, *Journal of Physics and Chemistry of Solids*, 2023, 180, 111486, DOI: 10.1016/j.jpcs.2023.111486.
- [27] Singh, R. C., Singh, M. P., Singh, O., and Chandi, P. S, *Sensors and Actuators B: Chemical*, 2009, 143, 226-232, DOI: 10.1016/j.snb.2009.09.032.
- [28] Lee, S., Oh, S., and Oh, M, *Angewandte Chemie*, 2020, 132, 1343-1349, DOI: 10.1002/ange.201912986.
- [29] Cubillas, P., Anderson, M. W., and Attfield, M. P, *Chemistry–A European Journal*, 2012, 18, 15406-15415, DOI: 10.1002/chem.201202261.
- [30] Li, Z., Yang, J., Guang, T., Fan, B., Zhu, K., and Wang, X, *Small Methods*, 2021, 5, 2100193, DOI: 10.1002/smtd.202100193.
- [31] Lei, B., Cui, W., Sheng, J., Wang, H., Chen, P., Li, J., ... and Dong, F, *Science Bulletin*, 2020, 65, 467-476, DOI: 10.1016/j.scib.2020.01.007.
- [32] Aghaziarati, M., Yamini, Y., and Shamsayei, M, *Microchimica Acta*, 2020, 187, 118, DOI: 10.1007/s00604-019-4102-5.
- [33] Hussain, M. B., Kang, B., Cheng, X., Ma, C., Wang, X., Mehmood, R., and Iqbal, S, *International Journal of Hydrogen Energy*, 2023, 48, 13780-13790, DOI: 10.1016/j.ijhydene.2022.12.296.
- [34] Chen, X., Peng, X., Jiang, L., Yuan, X., Fei, J., and Zhang, W, *Chemical engineering journal*, 2022, 427, 130945, DOI: 10.1016/j.cej.2021.130945.
- [35] Ahila, M., Subramanian, E. D. P. P., and Pathinettam Padiyan, D, *Journal of Electroanalytical Chemistry*, 2017, 805, 146-158, DOI: 10.1016/j.jelechem.2017.10.037.
- [36] Nayak, S. K., Pradhan, S. K., Panda, S., Bariki, R., and Mishra, B. G, *Applied Catalysis B: Environment and Energy*, 2025, 360, 124534, DOI: 10.1016/j.apcatb.2024.124534.
- [37] Shah, A., Saleem, S., Amin, N. U., Salman, M., Ling, Y., Khesro, A., and Khan, M, *Materials Science and Engineering: B*, 2023, 294, 116508, DOI: 10.1016/j.mseb.2023.116508.



- [38] Zhang, F., Zhang, T., Yang, X., Zhang, L., Leng, K., Huang, Y., and Chen, Y, Energy & Environmental Science, 2013, 6, 1623-1632, DOI: 10.1039/C3EE40509E.
- [39] Ma, Y., Bai, Y., Liang, B., Yang, R., Zheng, S., Hu, C., ... and Wei, L, Colloids and Surfaces A: Physicochemical and Engineering Aspects, 2022, 633, 127896, DOI: 10.1016/j.colsurfa.2021.127896.
- [40] Li, J., Wu, Q., and Zan, G, European Journal of Inorganic Chemistry, 2015, 2015, 5751-5756, DOI: 10.1002/ejic.201500904.
- [41] Mbam, S. M., Obodo, R. M., Apeh, O. O., Nwanya, A. C., Ekwealor, A. B. C., Nwulu, N., and Ezema, F. I, Journal of Materials Science: Materials in Electronics, 2023, 34, 1405, DOI: 10.1007/s10854-023-10835-7.
- [42] Mane, S. A., Kashale, A. A., Kamble, G. P., Kolekar, S. S., Dhas, S. D., Patil, M. D., ... and Ghule, A. V, Journal of Alloys and Compounds, 2022, 926, 166722, DOI: 10.1016/j.jallcom.2022.166722.
- [43] Yang, S., Qian, L., Ping, Y., Zhang, H., Li, J., Xiong, B., ... and He, C, Ceramics International, 2021, 47, 8290-8299, DOI: 10.1016/j.ceramint.2020.11.190.
- [44] Shinde, N. M., Xia, Q. X., Yun, J. M., Shinde, P. V., Shaikh, S. M., Sahoo, R. K., ... and Kim, K. H, Electrochimica Acta, 2019, 296, 308-316, DOI: 10.1016/j.electacta.2018.11.044.
- [45] Devi, N. A., Sinha, S., Nongthombam, S., and Swain, B. P, Materials Science in Semiconductor Processing, 2022, 137, 106212, DOI: 10.1016/j.mssp.2021.106212.



Data Availability

View Article Online
DOI: 10.1039/D5YA00376H

The data supporting the findings of this study are available within the article and its Electronic Supplementary Information (ESI). Additional raw data are available from the corresponding author upon reasonable request.

